

Crucial Role of Solvent and Additive During the Transformation of Liquid to Solid Polymer Electrolyte for Stabilizing 4.8 V Class $\text{LiCo}_{0.9}\text{Fe}_{0.1}\text{PO}_4$ Cathode in Anode and Anodeless Assemblies

Sreekumar Sreedeeep, Karayi Mangat Athira, Yun-Sung Lee,* and Vanchiappan Aravindan*

Here, a new class of solid electrolyte is successfully demonstrated, the so-called gel-solid polymer electrolyte (G-SPE), for the stabilization of high-voltage cathodes. This work aims to optimize the suitable G-SPE configuration, wherein different electrolyte combinations have been experimented with by varying the solvent and introducing additives. Further, the study has been extended for the stabilization of high-voltage cathodes like solid-state synthesized $\text{LiCo}_{0.9}\text{Fe}_{0.1}\text{PO}_4$ (LCFP) and commercial $\text{LiNi}_{0.5}\text{Mn}_{1.5}\text{O}_4$ (LNMO), wherein the electrolyte combinations of G-SPE_B-EL_LIDFOB and G-SPE_B-EL_FEC show excellent electrochemical performance. The *in situ* impedance analysis has been carried out to analyze the stability of the gel-polymer interface, wherein RCT exhibits a stable magnitude even as the cycling progresses to the 50th and 100th cycle. The post-XPS analysis of the electrode shows a stable LiF-rich solid electrolyte interphase layer on the electrode surface, showing the formation of a stable and robust layer enabled by LIDFOB along with the gel. In addition, the optimized G-SPE_B-EL_LIDFOB electrolyte combination has been further utilized for the fabrication of full- and anode-less cell configurations against $\text{Li}_4\text{Ti}_5\text{O}_{12}$ (LTO) and Cu as counter electrodes, respectively.

warming and climatic changes to a certain extent. With the surge in the demand for EVs, research and development among LIBs to fit the current requirements are gaining a lot of importance. Current research on LIBs mainly focuses on improving their energy density, proportional to the operating potential and specific capacity. Although specific capacity is intrinsic to a material, subtle changes can be made by various strategies such as surface coating, doping, etc., while improving the operating potential can significantly impact the energy density. Since the cathode possesses a high operating potential compared to anodes, the cathodic compartment significantly contributes to the overall energy density of LIBs.^[1,2] However, conventional cathodes, such as LiCoO_2 (LCO), $\text{LiNi}_x\text{Mn}_y\text{Co}_z\text{O}_2$ (NMC), and LiFePO_4 (LFP), operate at a lower potential, reducing the overall energy density of the LIBs.^[3–7] Hence, current research is focused on developing high-voltage cathodes, particularly spinel- $\text{LiNi}_{0.5}\text{Mn}_{1.5}\text{O}_4$ (LNMO) and olivine- LiCoPO_4 (LCP).^[8–11] The salient features of LNMO, including its high theoretical capacity ($\approx 150 \text{ mAh g}^{-1}$), high operating potential ($\approx 4.8 \text{ V vs. Li}$), high energy density, and environmental friendliness, have attracted a lot of attention as a promising high-voltage cathode. In addition, LCP, with its excellent theoretical capacity (167 mAh g^{-1}), high operating potential ($\approx 4.8 \text{ V vs. Li}$), high energy density ($\approx 720 \text{ Wh kg}^{-1}$), and high thermal stability due to a strong P–O covalent bond, is also worth mentioning.^[8,12] In contrast, the development of high-voltage cathodes is impeded due to various setbacks, of which poor electrolyte stability leading to its decomposition at high operating potential is more severe. Although carbonate electrolytes are widely employed in LIBs, the poor electrolyte stability window ($\approx 4.5 \text{ V vs. Li}$), causing its decomposition, limits its applicability to high-voltage cathodes. Also, using liquid electrolytes poses severe safety issues that can lead to thermal runaway. Hence, the requirement for an alternate electrolyte system has led to the advancement of the so-called solid-state electrolytes (SSE).^[13,14] Compared to liquid electrolytes, SSEs possess a high electrochemical stability window, high energy and power

1. Introduction

The invention of lithium-ion batteries (LIBs) has made a significant contribution to the sustainable development of the modern world. The transition toward emission-free electric vehicles is one such instance, as its introduction has reduced the overuse of fossil fuels, thereby minimizing the detrimental effect of global

S. Sreedeeep, K. M. Athira, V. Aravindan
Department of Chemistry
Indian Institute of Science Education and Research (IISER)
Tirupati, Andhra Pradesh 517619, India
E-mail: aravindan@iisertirupati.ac.in
Y.-S. Lee
School of Chemical Engineering
Chonnam National University
Gwang-ju 61186, Republic of Korea
E-mail: leeys@chonnam.ac.kr

The ORCID identification number(s) for the author(s) of this article can be found under <https://doi.org/10.1002/sml.202503310>

DOI: 10.1002/sml.202503310

density, and excellent thermal and mechanical stability. Also, the absence of metal dendrite formation mitigates the safety issues that are common among liquid electrolytes. Although possessing these advantages, the commercialization of SSEs has not yet been achieved due to various setbacks, such as high interface resistance, poor contact due to solid-solid interface, and poor ionic conductivity. Also, the high cost of the raw materials and poor scalability further limit its applicability in various battery systems.

The SSEs are classified based on the type of materials used as inorganic, and organic polymer-based SSEs. The inorganic SSEs are one of the widely explored SSEs owing to their high potential stability, excellent ionic conductivity (10^{-2} – 10^{-4} S cm $^{-1}$), and wide temperature application. The inorganic SSEs consist of oxide-based (Garnet (Li $_7$ La $_3$ Zr $_2$ O $_{12}$ (LLZO)), sodium superionic conductor (NASICON), and crystalline perovskite), sulfide-based (Li $_{10}$ GeP $_2$ S $_{12}$ (LGPS)), halide-based (Li $_3$ YCl $_6$, Li $_3$ YBr $_6$), and Hydroborate/Boro-Based SSEs. Polymer electrolytes, also called solid polymer electrolytes (SPEs), are the second class of SSEs that are gaining immense research importance owing to their high flexibility and ease of processability.^[15–20] In addition, it also mitigates the Li-dendrite formation causing thermal runaway. In the case of SPEs, the Li-salts undergo dissociation, forming cations and anions, while the Li-ions propagate through the polymer skeleton. Therefore, polymers with high dielectric constants are optimized for synthesizing SPEs, facilitating the Li-salt dissociation and improving Li-ion mobility. Polymers such as polyacrylonitrile (PAN), polymethylmethacrylate (PMMA), and polyvinyl alcohol (PVA) are widely used as polymer matrices for the SPEs. However, the poor electrode-electrolyte contact remains a major setback to hinder the development of SPEs.^[21,22]

To mitigate these setbacks, several strategies have been implemented, prominent among which are the use of functional fillers and the formation of an artificial interlayer. The use of fillers is a commonly employed strategy wherein the fillers provide additional channels for ion transport, thereby enhancing the conduction of ions. In addition, the fillers also enhance the flexibility and thermal properties of the electrolyte. There are various types of fillers, such as inorganic (TiO $_2$, Al $_2$ O $_3$, & BN), organic (MOF, & COF), and ceramic fillers (Li $_7$ La $_3$ Zr $_2$ O $_{12}$ (LLZO), Li $_{6.4}$ La $_3$ Zr $_{1.4}$ Ta $_{0.6}$ O $_{12}$, Li $_{10}$ GeP $_2$ S $_{12}$, and Li $_{3.25}$ Ge $_{0.25}$ P $_{0.75}$ S $_4$).^[15,18,21–23] Formation of an artificial interlayer through a polymerization method is another strategy wherein the monomer is transformed into a gel interface by a one-step polymerization strategy using various mechanisms, which include thermal-mediated, UV-irradiation-mediated polymerization, etc. Ring-opening polymerization (ROP) is one of the widely investigated types of *in situ* polymerization.^[24–28] Chen *et al.*^[29] reported a cationic ring-opening polymerization (CROP) of the oxetane ring group utilizing lithium bis(fluorosulfonyl)imide (LiFSI) as a catalyst. The same exhibited high ionic conductivity of 0.25 and 1.3 mS cm $^{-1}$ at 30 and 80 °C, and comparable oxidation stability of \approx 3.75 V vs. Li. The favorable aspect of ROP is its ability to produce the polymer with the equivalent composition and functionality as that of the monomers. Zhang *et al.*^[30] reported an *in situ* thermal polymerization strategy for the polymerization of a single-chain Poly(ethylene glycol) diacrylate (PEGDA) and Ethoxylated trimethylolpropane triacrylate (ETPTA) into a gel. The same has been utilized for the stabilization of LiFePO $_4$,

which shows an initial discharge capacity of 136 mAh g $^{-1}$ with a capacity retention of 84.62% after 800 cycles. However, the lack of productive monomers yielding high-voltage stable polymers limits their applicability to high-voltage LIBs.

Considering the various aspects of SSEs, this work depicts a new type of electrolyte combination by incorporating the desirable features of gel- and solid-polymer electrolyte, also called gel-solid polymer electrolyte (G-SPE). In this hybrid electrolyte, the gel-polymer electrolyte is formed by the polymerization of liquid into a gel electrolyte, where the ethylene carbonate (EC) component of the electrolyte is polymerized by an *in situ* radical-assisted ROP into polyethylene carbonate (PEC) under the neutral condition on a PVdF-HFP-BN, SPE support. In the G-SPE, the gel-polymer component improves the interfacial contact between the electrode and electrolyte, thereby mitigating the interfacial resistance and improving the contact between the electrode and the electrolyte. Also, as a liquid electrolyte is converted into a gel, electrolyte engineering has been carried out within the liquid electrolyte by changing the solvent and electrolyte additives to understand its effect on the stability of the gel interface. The SPE component of the G-SPE improves the flexibility and enhances the high-voltage stability of the electrolyte. Further, the BN filler in the SPE provides additional channels for the Li-ion migration, thereby enhancing the ionic conductivity. The high voltage stability of these electrolytes is depicted by the half-cell electrochemical studies with high-voltage cathodes such as LiCo $_{0.9}$ Fe $_{0.1}$ PO $_4$ @C and validated with spinel LiNi $_{0.5}$ Mn $_{1.5}$ O $_4$ as well. In addition, the full- and anode-less cell study of the optimized electrolyte combination has been carried out by coupling the LiCo $_{0.9}$ Fe $_{0.1}$ PO $_4$ @C against Li $_4$ Ti $_5$ O $_{12}$ (LTO) and Cu strip.

2. Results and Discussion

2.1. Material Characterizations

X-ray diffraction analysis (Figure 1a) of LCFP aligns well with the characteristic diffraction peaks of LiCoPO $_4$, with prominent diffraction at crystal planes of (011), (111), (200), (131), (211), (112), and (222) at 2θ values of 20.86, 25.83, 30.23, 35.99, 36.98, and 52.95, showing the formation of olivine phased rhombohedral LiCoPO $_4$. However, diffraction peaks corresponding to LFP can't be observed in the XRD spectra of LCFP due to its low concentration of Fe. The XRD spectra of PVdF-HFP-BN (Figure S1a, Supporting Information) show peaks corresponding to (020) and (002) crystal planes at 2θ values of 20.37 and 27.01, denoting the PVdF-HFP polymer matrix. The XPS survey spectra (Figure 1c) shows the surface elemental composition of Li, Co, Fe, P, O, and C in LCFP. Further, the deconvolution of Co 2p, Fe 2p, and C 1s core levels (Figure 1d–f) shows the chemical state of the elements. The C 1s core-level on deconvolution exhibits peaks corresponding to C—C (285.6 eV) and C = C (284.2 eV) functionalities. Also, the transition metal peaks corresponding to Co (Co 2p $_{1/2}$ and Co 2p $_{3/2}$) and Fe (Fe 2p $_{1/2}$ and Fe 2p $_{3/2}$) reveal their oxidation state to be +2. The BET analysis (Figure S1c, Supporting Information) of the PVdF-HFP-BN film exhibits surface area and pore volume of 62.94 m 2 g $^{-1}$ and 0.080 cm 3 g $^{-1}$. The large surface area and pore volume of the PVdF-HFP-BN promote effective percolation of the liquid electrolyte into the film, which further transforms it into a gel interface. The thermal stability of

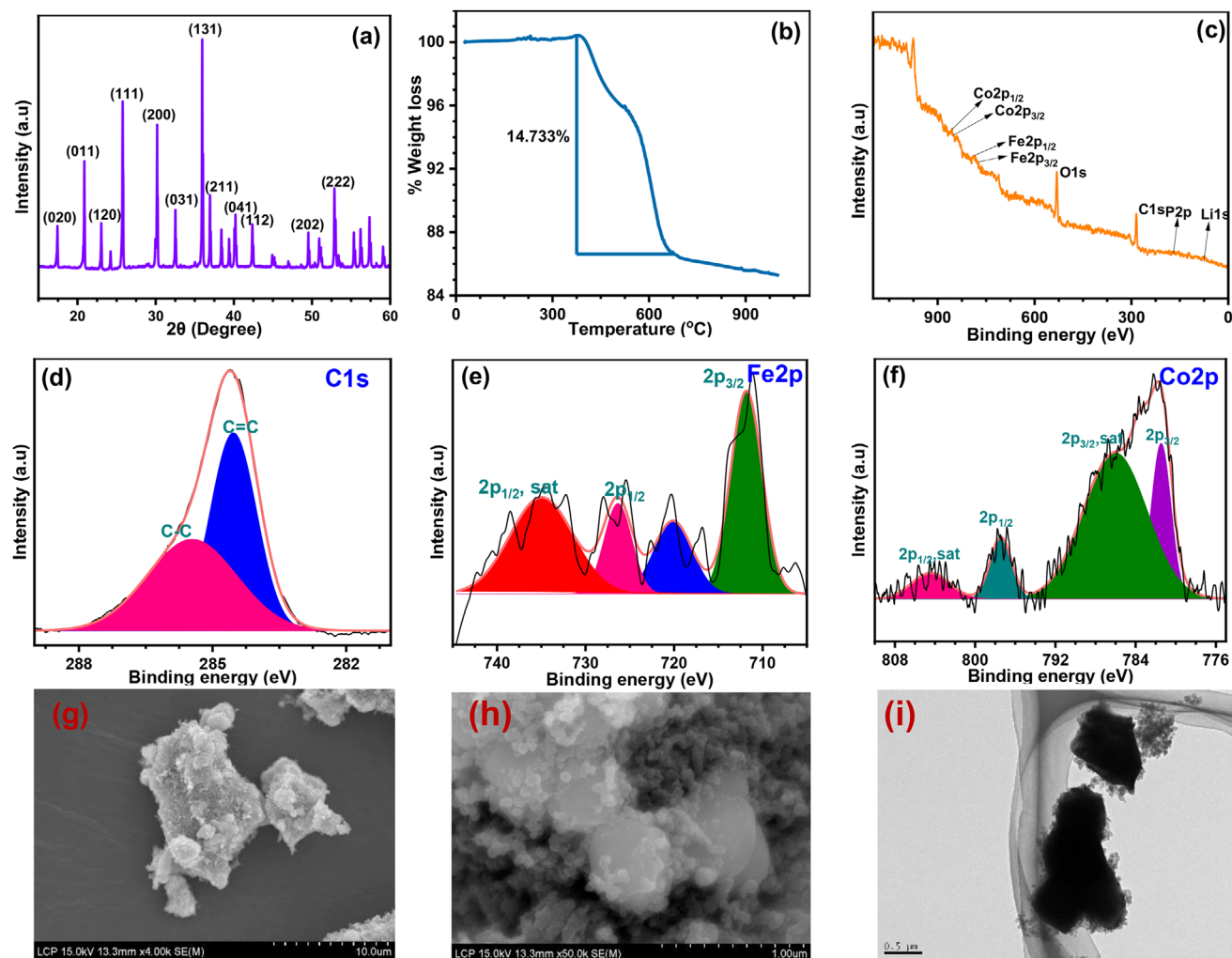


Figure 1. a) XRD spectra, b) TGA,^[31] c–f) XPS survey spectra, and deconvoluted spectra of C 1s, Fe 2p, and Co 2p of LCFP, g,h) FE-SEM, and i) TEM images of LCFP.

the PVdF-HFP-BN, determined from the TGA analysis (Figure S1b, Supporting Information), shows a weight loss of $\approx 44.63\%$ due to the decomposition of the organic functionalities in the film. On the other hand, the LCFP (Figure 1b) shows a weight loss of 14.63%, which illustrates the decomposition of the carbon layer on the material. The morphology and structure of the LCFP have been elucidated from the FE-SEM and TEM analysis. The FE-SEM images (Figure 1g,h) of LCFP show agglomeration of the particles. However, the TEM image (Figure 1i) of the LCFP shows the carbon coating on its surface. Further, the interlayer spacing of the LCFP has been determined from the TEM image to be ≈ 0.329 nm.

The formation of a gel interface is highly dependent on the polymerization of EC into polyethylene carbonate (PEC), and this is the first report on the radical-assisted ring-opening polymerization (ROP) of EC into PEC in a neutral medium. The mechanism for ROP can be elucidated from the NMR spectra of the electrolyte. The ^1H -NMR spectra of the electrolyte during the propagation of the ROP are shown in Figure S2a (Supporting Information). The ^1H -NMR spectra of the unpolymerized electrolyte de-

pict a peak corresponding to the monomer EC at a chemical shift value of $\delta \approx 4.6$ ppm. On thermal treatment, the ^1H -NMR spectra show a rise in a highly up-field signal at $\delta \approx 3.6$ ppm, which corresponds to the $\text{CH}_2\text{-d}$ proton within the ether-linkage of the PEC. Now, as the polymerization completes, the $\text{CH}_2\text{-d}$ ($\delta \approx 3.6$ ppm) signal becomes more intense compared to the signal corresponding to the EC. In addition, a complete conversion of EC to PEC can be observed as the reaction progresses further. Similarly, the ^{13}C -NMR spectra (Figure S2b, Supporting Information) exhibit four different signals that correspond to the formation of PEC. The highly downfield signal at $\delta \sim 158$ ppm denotes the carbonyl carbon atom, $\text{C}=\text{O}$ (b). On the other hand, the intense signal at $\delta \sim 65$ ppm denotes the $\text{CH}_2\text{(a)}$ carbon atom adjacent to the carbonate functionality, while the less intense signals at $\delta \sim 67$ ppm denote the $\text{CH}_2\text{(c)}$ carbon atom, adjacent to $\text{CH}_2\text{(a)}$ carbon atom. Also, the signal at $\delta \sim 70$ ppm corresponds to the $\text{CH}_2\text{(d)}$ carbon atom within the ethereal linkage. Hence, the NMR further elucidated the fact that radical-assisted ROP highly contributes to the formation of a gel-polymer interface between the electrode and the SPE.

A temperature-dependent Raman study (Figure S3, Supporting Information) has been further carried out to understand the gelation process of the liquid-to-gel electrolyte at different temperatures ranging from 10 to 80 °C. At moderate temperatures ranging from 10 to 60 °C, characteristic peaks corresponding to the formation of PEC cannot be observed, hence showing that no liquid-to-gel transformation has occurred within these temperatures. On the other hand, as the temperature is increased to 70 °C, a new peak can be observed at $\approx 2959\text{ cm}^{-1}$, which shows the polymerization of EC into PEC. Upon further increasing the temperature to 80 °C, the intensity of the PEC peak further increases, which shows the completion of the phase change. Hence, the temperature-dependent Raman study confirms the occurrence of a phase change in the electrolyte.

2.2. Theoretical Study of the G-SPE

The stability of the different electrolyte combinations has been determined from the energy gap (ΔE), also called the electrolyte stability window, between the highest occupied molecular orbital (HOMO) and lowest unoccupied molecular orbital (LUMO) of each of the electrolyte components. Therefore, the larger the ΔE for each of the electrolyte components, the higher the electrolyte stability. Further higher the LUMO level larger will be the reduction potential, while lower the HOMO level higher will be the reduction potential. The HOMO–LUMO energy level diagram depicts an enhancement in the ΔE value among the various solvent molecules, while the electrolyte additives show a narrow energy gap. Based on the magnitude of ΔE , wherein ΔE_{DEC} , ΔE_{DMC} , ΔE_{EMC} , ΔE_{EC} , ΔE_{FEC} , and ΔE_{LiDFOB} signifies the energy gap between DEC, DMC, EMC, EC, FEC, and LiDFOB, the electrolyte stability window of the different electrolyte components (Figure S4, Supporting Information) can be arranged as $\Delta E_{\text{DMC}} > \Delta E_{\text{DEC}} > \Delta E_{\text{EMC}} > \Delta E_{\text{EC}} > \Delta E_{\text{FEC}} > \Delta E_{\text{LiDFOB}}$. The lower energy gap of the LiDFOB and FEC promotes preferential oxidation and reduction compared to other electrolyte components. Further, the smaller magnitude of ΔE_{LiDFOB} compared to ΔE_{FEC} further illustrates the fact that LiDFOB is more prone to electrolyte decomposition, forming a stable solid electrolyte interphase (SEI) layer compared to FEC. In addition, among the different solvents, the DMC exhibits a higher electrolyte stability window than DEC and EMC. Hence, based on a theoretical perspective, the electrolyte stability window of the different electrolyte combinations follows the order given by G-SPE_B-EL_LiDFOB > G-SPE_B-EL_FEC > G-SPE_B-EL > G-SPE_EC_DEC > G-SPE_EC_EMC. Furthermore, the charge distribution of the various electrolyte components has been determined from the electrostatic potential (ESP) diagram (Figure S5, Supporting Information), wherein a uniform charge distribution can be observed among the different electrolyte components.

2.3. Electrochemical and Physical Properties of the Electrolyte

The mobility of the Li-ions within the G-SPE is another important parameter that has to be determined. The evaluation of the Li-ion conduction has been carried out from the electrochemical

impedance spectra (EIS) of the different electrolyte combinations using the equation-

$$\sigma = \frac{L}{R_b A} \quad (1)$$

Where σ is the Li-ion conduction parameter, L is the thickness of the electrolyte, R_b is the bulk resistance, and A is the cross-section area of the electrolyte. The magnitude of σ for the different electrolyte combinations is found to be 9.5, 8.2, 7.5, 6.1, and 4.2 mS cm^{-1} , respectively, for G-SPE_B-EL_LiDFOB, G-SPE_B-EL_FEC, G-SPE_B-EL, G-SPE_EC_DEC, and G-SPE_EC_EMC. The ionic conductivity is proportional to the number of free Li-ions present in the system by the dissociation of the LiPF_6 . The rate at which LiPF_6 undergoes dissociation to Li^+ and PF_6^- is highly dependent on the polarity of the solvent, defined by the dielectric constant, ϵ . Among the solvents used here, the EC ($\epsilon = 89.8$) has the highest ϵ -value followed by the DMC ($\epsilon = 3.1$), then DEC ($\epsilon = 2.8$), and finally EMC ($\epsilon = 2.4$). Based on the dielectric constant, the polarity of the different electrolyte combinations follows the given trend: EC_DMC > EC_DEC > EC_EMC. Therefore, a similar trend can be observed in the case of the rate of formation of free Li-ions and, hence, the ionic conductivity. In addition, the use of LiDFOB as an additive in EC_DMC can exceptionally improve the Li-ion conductivity due to the presence of additional free Li-ions from LiDFOB, which, along with the Li-ions from LiPF_6 , can enhance the ionic conductivity of the electrolyte. The use of FEC in EC_DMC can also improve the ionic conductivity by enhancing the solvent polarity, which further improves the number of free Li-ions, thereby improving the ionic conductivity. Hence, a similar trend of ionic conductivity in liquid electrolytes is imparted to the G-SPE. Therefore, the trend in ionic conductivity of the given electrolyte systems in gel-polymer state is given by: G-SPE_B-EL_LiDFOB > G-SPE_B-EL_FEC > G-SPE_EC_DEC > G-SPE_EC_EMC.

The transference number (t_{Li^+}) for the different electrolyte combinations (Figure 2b,d,f,h,i) has been evaluated from the symmetric cell configuration of $\text{Li}\backslash\text{G-SPE}\backslash\text{Li}$ from the combination of EIS with DC-chronoamperometry, using the Bruce-Vincent equation, given by

$$t_{\text{Li}^+} = \frac{I^{\text{ss}} (\Delta V - I^0 R_i^0)}{I^0 (\Delta V - I^{\text{ss}} R_i^f)} \quad (2)$$

Where I^{ss} is the steady-state current, I^0 is the initial current applied, R_i^0 is the initial resistance, R_i^f is the final resistance, and ΔV is the applied polarization potential. The as-determined magnitudes of t_{Li^+} are 0.83, 0.80, 0.77, 0.75, and 0.71 for gel-polymer electrolyte combinations of G-SPE_B-EL_LiDFOB, G-SPE_B-EL_FEC, G-SPE_B-EL, G-SPE_EC_DEC, and G-SPE_EC_EMC, respectively. This trend in the t_{Li^+} is in complete agreement with the determined magnitudes of the ionic conductivity.

The stability of the different electrolyte combinations has been evaluated from the symmetric cell study with the cell configuration of $\text{Li}\backslash\text{G-SPE}\backslash\text{Li}$ (Figure 2a,c,e,g,i) carried out at an areal current density of 0.5 mA cm^{-2} . The symmetric cell study shows stable cycling among the symmetric cells with G-SPE_B-EL_LiDFOB and G-SPE_B-EL_FEC electrolyte, with stability to

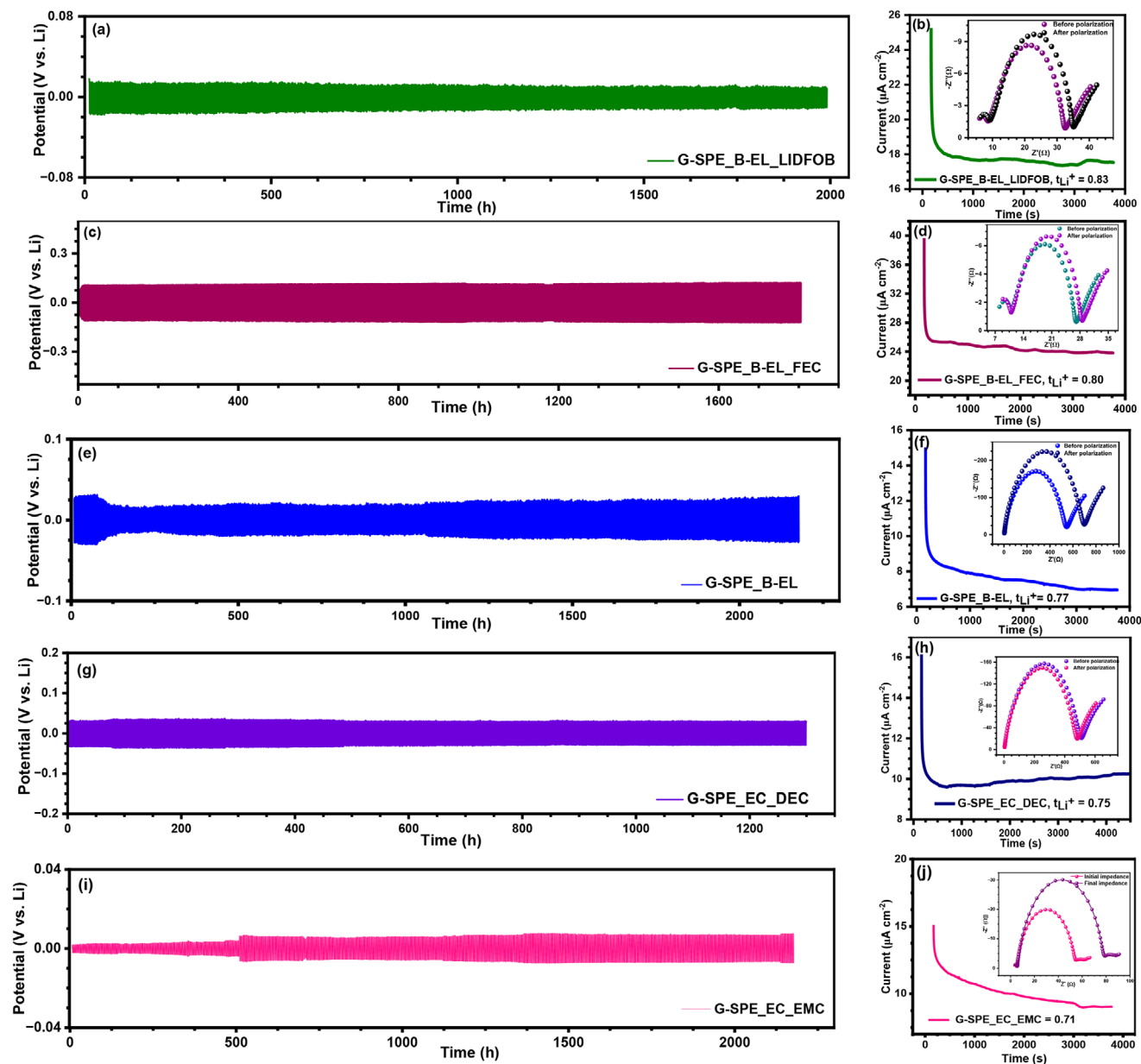


Figure 2. Symmetric cell studies showing the stability and transference number of a,b) G-SPE_B-EL_LiDFOB, c,d) G-SPE_B-EL_FEC, e,f) G-SPE_B-EL, g,h) G-SPE_EC_DEC, and i,j) G-SPE_EC_DMC.

a duration of 2000 and 1900 h, respectively. In addition, both of these electrolytes do not exhibit any polarization as the cycling progresses. This can be attributed to the formation of a stable SEI layer by the LiDFOB and FEC components, thereby preventing further electrolyte decomposition and improving the stability of the gel interface between the electrode and the SPE. In contrast, the G-SPE_B-EL shows initial polarization to 200 cycles and attains stability as the cycling progresses, showing stable cycling up to 2000 h. Similarly, G-SPE_EC_DEC also shows initial polarization, while compared to G-SPE_EC_DMC, it is stable up to a duration of 1200 h only. The reason for the polarization among these electrolytes is electrolyte decomposition, which detrimentally affects the stability of the electrolyte. However,

the G-SPE_EC_DMC exhibits large polarization during the initial and final stages of electrochemical cycling, showing its poor electrolyte stability. Hence, the electrolyte combinations forming stable gel interfaces are optimized to be G-SPE_B-EL_LiDFOB and G-SPE_B-EL_FEC. The stability of the optimized G-SPE_B-EL_LiDFOB has been analyzed at different current densities of 0.1, 0.5, and 1 mA cm⁻². The symmetric cell plot (Figure S6, Supporting Information) of the G-SPE_B-EL_LiDFOB exhibits stable cycling at high current densities of 1 mA cm⁻² without any polarization, hence showing the compatibility of the electrolyte to fast charging and discharging.

The oxidation stability of the different electrolyte combinations was investigated by an asymmetric cell configuration of

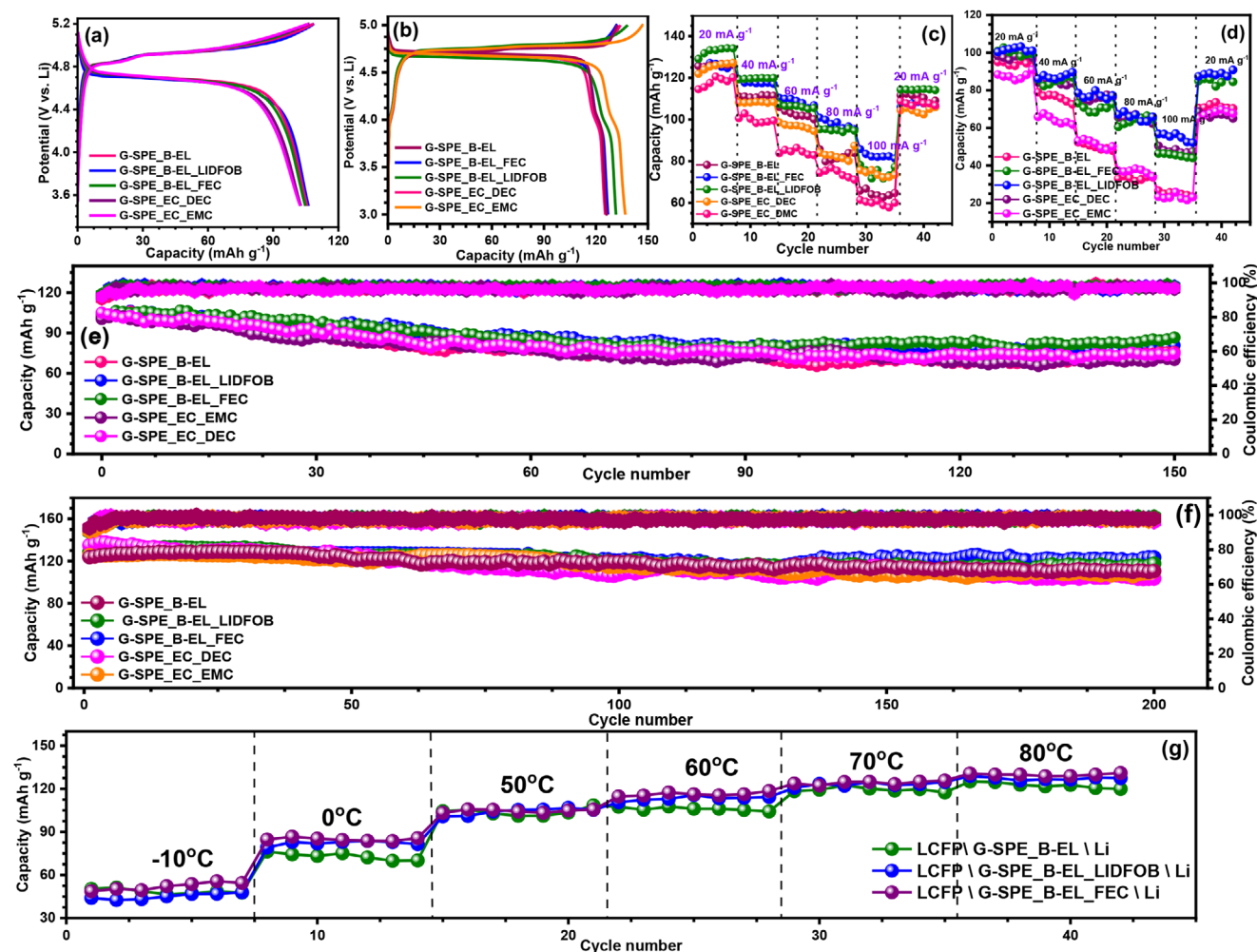


Figure 3. Charge–discharge plots for a) LCFP and b) LNMO, c,d) rate-performance profile for LCFP and LNMO, e,f) capacity vs. cycle number plot for LCFP and LNMO, and g) temperature study for LCFP from -10 to 80 °C.

Li/G-SPE\SS using the linear sweep voltammetry (LSV) technique. The LSV (Figure S7a, Supporting Information) of the G-SPE_B-EL exhibits enhanced oxidation stability to a potential of up to ≈ 4.8 V vs. Li. The addition of FEC and LiDFOB into the G-SPE_B-EL forming G-SPE_B-EL_FEC and G-SPE_LiDFOB further enhances the oxidation stability to ≈ 5.1 and 5.7 V vs. Li, respectively. This improvement in the oxidation stability of G-SPE_B-EL_FEC and G-SPE_LiDFOB can be attributed to the formation of a stable SEI layer along with the gel, thereby improving its interfacial stability even at high operating potential. Hence, this further shows the role of electrolyte additives in enhancing the interfacial stability of the G-SPE.

The Li-ion transfer kinetics of the G-SPEs were analyzed based on the magnitudes of activation energy (E_a) evaluated from the Arrhenius plot (Figure S7b, Supporting Information). The as-determined magnitudes of E_a are 0.27, 0.39, 0.66, 0.75, and 0.84 eV, respectively, for G-SPE_B-EL_LiDFOB, G-SPE_B-EL_FEC, G-SPE_B-EL, G-SPE_EC_DEC, and G-SPE_EC EMC. As the magnitude of E_a increases, a corresponding decrease in the Li-ion kinetics occurs. Hence, the G-SPE_EC EMC exhibits a poor rate of Li-ion kinetics, while G-SPE_B-EL_LiDFOB shows enhanced

Li-ion kinetics, which further supports the trend in the ionic conductivity and transference number. The fire retardancy of the G-SPEs has been further depicted by the flammability test (Figure S8, Supporting Information) of the electrolytes. The G-SPE_B-EL_LiDFOB and G-SPE_B-EL_FEC depict excellent fire-resistant behavior to a duration of 5, 10, 15, and 20 s, hence showing that the as-formulated G-SPE is a better counterpart for the next generation solid electrolytes.

2.4. Half-Cell Studies with LCFP and LNMO as Cathode

To understand the efficiency of G-SPEs at higher operating potentials, the half-cell performance has been conducted for both cathodes with different G-SPE electrolytes. The half-cell studies of solid-state synthesized LCFP and commercial LNMO were conducted within a potential window of 3.5–5.2 and 3.5–5 V vs. Li. The half-cell studies of the LCFP (Figure 3a,e) exhibit excellent electrochemical performance with discharge capacities of 107, 106, 104, 103, and 102 mAh g⁻¹ with capacity retention of 80%, 74%, 82%, 69%, and 70% and coulombic efficiency of

98%, 97%, 98%, 96%, and 95% after 150 cycles for G-SPE_B-EL-LiDFOB, G-SPE_B-EL, G-SPE_B-EL-FEC, G-SPE_EC_DEC, and G-SPE_EC EMC, respectively. Further, the electrochemical studies have been extended to commercial LNMO cathode (Figure 3b,f), which exhibits a similar trend in the electrochemical properties as that of LCFP with initial discharge capacities of 137, 132 (LiDFOB), 128 (FEC), 127 (DEC), and 125 (B-EL) mAh g⁻¹ with capacity retentions of 74%, 89%, 87%, 76%, and 71% and coulombic efficiencies 94%, 99%, 98%, 96%, and 97% after 200 cycles for G-SPE_EC EMC, G-SPE_B-EL-LiDFOB, G-SPE_B-EL-FEC, G-SPE_EC_DEC, and G-SPE_B-EL. The enhancement in the electrochemical performance among G-SPE_B-EL-FEC and G-SPE_B-EL-LiDFOB can be attributed to the formation of a stable SEI layer, which improves the stability of the formed gel interface and enhances the high-voltage stability, thereby mitigating the electrolyte decomposition. Further, the rate performance study of LCFP (Figure 3c) and LNMO (Figure 3d) shows superior electrochemical performance among the G-SPE_B-EL-LiDFOB and G-SPE_B-EL-FEC with excellent capacity retention of 86 and 85% in LCFP and 88 and 90% in LNMO even after cycling at very high current densities. Further, the temperature studies of the LCFP have been carried out to investigate its practical applicability in different climatic conditions. From the cycling profile, it is interesting to note that the LCFP exhibits superior electrochemical performance both at high and low temperatures (Figure 3g). At low temperatures, the LCFP exhibits excellent discharge capacities of 87, 82, and 70 mAh g⁻¹ at 0 °C and 54, 47, and 46 mAh g⁻¹ at -10 °C with superior cycle stability among the G-SPE_B-EL-LiDFOB, G-SPE_B-EL-FEC, and G-SPE_B-EL electrolyte combinations. Besides, at high temperatures, the LCFP exhibits enhanced discharge capacities of 126, 123, and 117 mAh g⁻¹ at 70 °C and 132, 127, and 119 mAh g⁻¹ at 80 °C, with better cycle stability for the G-SPE_B-EL-LiDFOB, G-SPE_B-EL-FEC, and G-SPE_B-EL electrolyte combinations. These results show that the as-formed gel interface by the PEC component completely stabilizes the electrolyte, making it stable even at high and low temperatures. Also, the enhanced stability among the G-SPE_B-EL-LiDFOB and G-SPE_B-EL-FEC can be attributed to the SEI layer formed by the decomposition of FEC and LiDFOB, providing additional stability to the gel interface. Hence, from the preliminary cell studies, G-SPE_B-EL-LiDFOB and G-SPE_B-EL-FEC have been optimized for further electrochemical studies.

The cyclic voltammetry (CV) (Figure S9a, Supporting Information) traces of LCFP and LNMO were performed at a scan rate of 0.1 mV s⁻¹. The LCFP shows oxidation and a reduction peak corresponding to the Co³⁺/Co²⁺ couple at 5.04 and 4.7 V vs. Li, respectively. However, the peak showing the oxidation/reduction of Fe cannot be observed in the CV, hence showing that Fe remains inactive and won't take part in the electrochemical reaction. In the case of LNMO, two pairs of oxidation and reduction peaks can be observed, which include oxidation peaks at 4.09 and 4.98 V vs. Li and reduction peaks at 4.42 and 3.93 V vs. Li, which corresponds to the Mn and Ni redox couples in the compound. Hence, it can be confirmed that the use of G-SPE does not hinder the electrochemical activity in both LCFP and LNMO.

Electrochemical impedance spectroscopy (EIS) (Figure S9b, Supporting Information) has been performed to analyze the mechanism and kinetics of the electrochemical reactions in-

involved. The equivalent circuit diagram corresponding to the given Nyquist plot is a combination of solution resistance (R_{Ω}), charge-transfer resistances R_1 and R_2 due to the SEI layer formation, constant phase elements Q_1 and Q_2 , in the high-frequency region, and a rising Warburg (W) tail at the low-frequency region. In addition, the magnitude of charge-transfer resistance (R_{CT}) for LCFP cycled in different electrolytes follows the given trend: G-SPE_B-EL-LiDFOB < G-SPE_B-EL-FEC < G-SPE_B-EL < G-SPE_EC_DEC < G-SPE_EC EMC. The high R_{CT} value among the G-SPE_EC EMC and G-SPE_EC_DEC can be attributed to the decomposition of the DEC and EMC components on charging to 5.2 V vs. Li due to its poor oxidation stability, leads to the formation of a thicker SEI layer along with gel interface, which further reduces the mobility of Li-ions. On the other hand, the sacrificial decomposition of FEC or LiDFOB prevents further decomposition of other electrolyte components upon initial charging, leading to the formation of a stable gel interface. Also, the as-formed gel interface is highly conductive and facilitates the movement of Li-ions during charge-discharge, thereby improving the electrochemical performance. Besides, the *in situ* impedance analysis (Figure S10, Supporting Information) of the LCFP cycled in G-SPE_B-EL-LiDFOB is also in agreement with the given statement, wherein the LCFP exhibits large R_{CT} value in the initial cycle due to the formation of the gel-polymer interface and also due to the decomposition of the LiDFOB forming an additional SEI layer on the polymerized gel. However, the as-formed SEI-polymer interface will stabilize as the cycling progresses; hence, a gradual decrement in the R_{CT} value can be observed in the 10th cycle. Furthermore, the magnitude of R_{CT} remains stable as the cycling progresses to 50th and 100th due to the stability of the as-formed SEI-polymer interface and lack of irreversibility. Therefore, the *in situ* impedance analysis is in direct agreement with the fact that the as-formed polymer interface remains stable even at high operating potential and also during deep cycles of charge-discharge.

The apparent diffusion coefficient has been evaluated from the Nyquist plot for the different electrolyte combinations coupled with LCFP as the cathode. The evaluation of the diffusion coefficient has been carried out from the slope of the Z vs. $\omega^{-1/2}$ graph (Figure S11, Supporting Information) using the equation given by^[32–35]

$$D_{Li} = \frac{R^2 T^2}{2A^2 n^4 F^2 C^2 \sigma^2} \quad (3)$$

Where D_{Li} is the diffusion coefficient of Li-ions, R is the universal gas constant (8.314 J K⁻¹ mol⁻¹), T is the temperature (298 K), A is the cross-sectional area of the electrode, n is the number of moles of Li-ions in charge-discharge, F is the faraday constant (96,485 C mol⁻¹), C is the concentration of electrolyte, and σ is the slope. The as-determined magnitudes of D_{Li} are 3.9×10^{-13} , 4.6×10^{-13} , 8.7×10^{-13} , 2.5×10^{-13} , and 1.9×10^{-13} m² s⁻¹ for G-SPE_B-EL, G-SPE_B-EL-FEC, G-SPE_B-EL-LiDFOB, G-SPE_EC_DEC, and G-SPE_EC EMC, respectively. The enhanced D_{Li} in the case of G-SPE_B-EL-FEC and G-SPE_B-EL-LiDFOB further shows that the SEI layer formed along with the gel interface facilitates the Li-ion kinetics compared to other electrolytes. In addition, G-SPE_EC EMC show a decrease in the magnitude of D_{Li} due to their poor oxidation stability of EMC, forming an unstable and

thicker gel-interface layer that blocks the mobility of Li-ions compared to G-SPE_EC_DEC and G-SPE_B-EL.

The post-analysis of the cycled LCFP electrode and the G-SPE has been carried out with the XPS analysis (Figures S12, S13, Supporting Information) to understand the mechanism of the electrochemical reaction and also the surface elemental composition on both electrode and electrolyte. The XPS analysis of the cycled LCFP electrode shows the surface elemental composition of elemental core levels, including P 2p, C 1s, O 1s, F 1s, Fe 2p, and Co 2p. The deconvolution of the P 2p core level gives peaks corresponding to Li_xPF_y (136 eV) and $\text{Li}_x\text{PO}_y\text{F}_z$ (134 eV), which corresponds to the decomposition products of the LiPF_6 .^[36–38] Also, the F 1s core level on deconvolution shows peaks corresponding to $\text{Li}_x\text{PO}_y\text{F}_z$ (683 eV) and LiF (686 eV). The $\text{Li}_x\text{PO}_y\text{F}_z$ and Li_xPF_y peaks correspond to the decomposition products that are formed by the hydrolysis of PF_6^- anion, while the LiF peak corresponds to the decomposition product of LIDFOB, forming a LiF-rich SEI layer. In addition, the insulating LiF coating will further prevent any attack by the nucleophile, thereby mitigating any transition metal dissolution. In addition, the deconvolution of B 1s core-level further elucidates the SEI layer, wherein the peak at 193.5 eV shows the precursor, $\text{LiBF}_2\text{C}_3\text{O}_3$, formed by the ring opening reaction of LIDFOB followed by the radical-based reaction with EC. In addition, the spectra further exhibit B-F functionality, illustrating the F^- scavenging nature of LIDFOB. The mechanism of LIDFOB decomposition shown in Scheme S1 (Supporting Information) further elaborates on the formation mechanism of SEI by LIDFOB, wherein LIDFOB undergoes decomposition through a radical-assisted path leading to the reaction with EC present in the electrolyte, forming a LiF-rich SEI layer. The C 1s core level also shows peaks corresponding to the $\text{O}=\text{C}=\text{O}$ (287.5 eV), $\text{C}=\text{O}$ (285.8 eV), and $\text{C}-\text{H}$ (284.4 eV), wherein the $\text{O}=\text{C}=\text{O}$ functionality corresponds to the oxalate decomposition product of the LIDFOB. Also, the transition metal peaks corresponding to Co 2p and Fe 2p do not show any variation in the oxidation state, with Co having an oxidation state of +3 and Fe in an oxidation state of +2, hence further elucidating the fact that no metal dissolution or parasitic side reactions occur during the charge-discharge.

The XPS spectra of the G-SPE_LIDFOB electrolyte have been performed further to elucidate the functionalities of the P 2p, C 1s, O 1s, and F 1s core levels. The deconvolution of the P 2p core level shows peaks corresponding to $\text{Li}_x\text{PO}_y\text{F}_z$ and P—O functionalities in the decomposed product of the PF_6^- anion. Also, the deconvolution of the F 1s core level shows a highly intense LiF peak, which can be attributed to the LiF-rich SEI layer formed by the LIDFOB. Also, the C 1s spectra show peaks corresponding to the decomposition products of LIDFOB, which include $\text{O}=\text{C}=\text{O}$, $\text{C}=\text{C}$, and $\text{C}=\text{C}$, while O 1s spectra show similar peaks, hence confirming the formation of these decomposition products on the gel interface. Additionally, the absence of any transition metal peaks in the electrolyte further depicts the elimination of transition metal dissolution accompanying the charge-discharge processes.

The FE-SEM (Figure S14, Supporting Information) images of the cycled and uncycled G-SPE_B-EL_LIDFOB have been carried out to understand its morphology. The FE-SEM images of both cycled and uncycled G-SPE do not show any difference in their surface morphology. This further proves the fact that the LiF-rich

SEI layer formed by the LIDFOB will prevent any degradation of the electrolyte, thereby providing excellent cycle stability for the LCFP cathode during cycling. Also, the EDS elemental mapping (Figure S15, Supporting Information) of the cycled G-SPE_B-EL_LIDFOB depicts a uniform distribution of F throughout the selected area due to the formation of a uniform LiF-rich SEI layer by the LIDFOB, while the uncycled G-SPE_B-EL_LIDFOB shows a non-uniform distribution of F. However, the EDS elemental mapping of C shows uniform distribution in both cycled and uncycled G-SPE_B-EL_LIDFOB.

2.5. Full- and Anode-Less Cell Study

The full cell fabrication has been carried out by pairing the LCFP against $\text{Li}_4\text{Ti}_5\text{O}_{12}$ (LTO) as anode (Figure 4a,b) with optimized G-SPE_B-EL_LIDFOB as the electrolyte, and the testing has been performed within a potential window of 1.5–2.6 V at a current density of 20 mA g^{-1} . The full cell depicted an excellent initial discharge capacity of 98 mAh g^{-1} with capacity retention and coulombic efficiency of 81 and 98% after 100 cycles. This enhanced electrochemical performance can be attributed to the SEI-containing gel-polymer interface formed by the decomposition of LIDFOB.

Anode-less cell configuration has also been carried out against a Cu strip as a counter electrode (Figure 4c,d), and the testing has been conducted within a potential range of 3–5.1 V at a current density of 20 mA g^{-1} with the electrolyte combination of G-SPE_B-EL_LIDFOB. The anode-less cell depicts an excellent discharge capacity of 96 mAh g^{-1} with capacity retention and coulombic efficiency of 84% and 97% after 100 cycles. These results are in complete agreement with the fact that the designed electrolyte configuration does not show decomposition even at high operating potential and can be a promising electrolyte for the development of high-voltage cathodes. Also, a comparison study of this work was conducted with previously reported works to elaborate further on its superiority (Tables T1 and T2, Supporting Information).

3. Conclusion

Here, we successfully demonstrated a new concept of gel-solid polymer electrolytes by incorporating the properties of both GPE and SPE, wherein we studied the effect of electrolyte solvents and additives on the formation of a stable gel interface. Among the different electrolyte configurations that have been studied, the G-SPE_B-EL_LIDFOB and G-SPE_B-EL-FEC exhibit excellent electrochemical properties, such as high ionic conductivity, diffusion coefficient, and high oxidation stability. Furthermore, the high-voltage stability of the optimized electrolytes was depicted by the superior electrochemical performance of the solid-state synthesized LCFP and commercial LNMO cathode materials. The *in situ* impedance analysis of the LCFP with G-SPE_B-EL_LIDFOB electrolyte exhibits stable R_{CT} as the cycling progresses, which further depicts the stability of the as-formed gel interface. Also, the XPS analysis of the cycled LCFP electrode further shows the formation of an insulating LiF-rich SEI layer by LIDFOB, thereby mitigating the transition metal dissolution by the nucleophilic attack

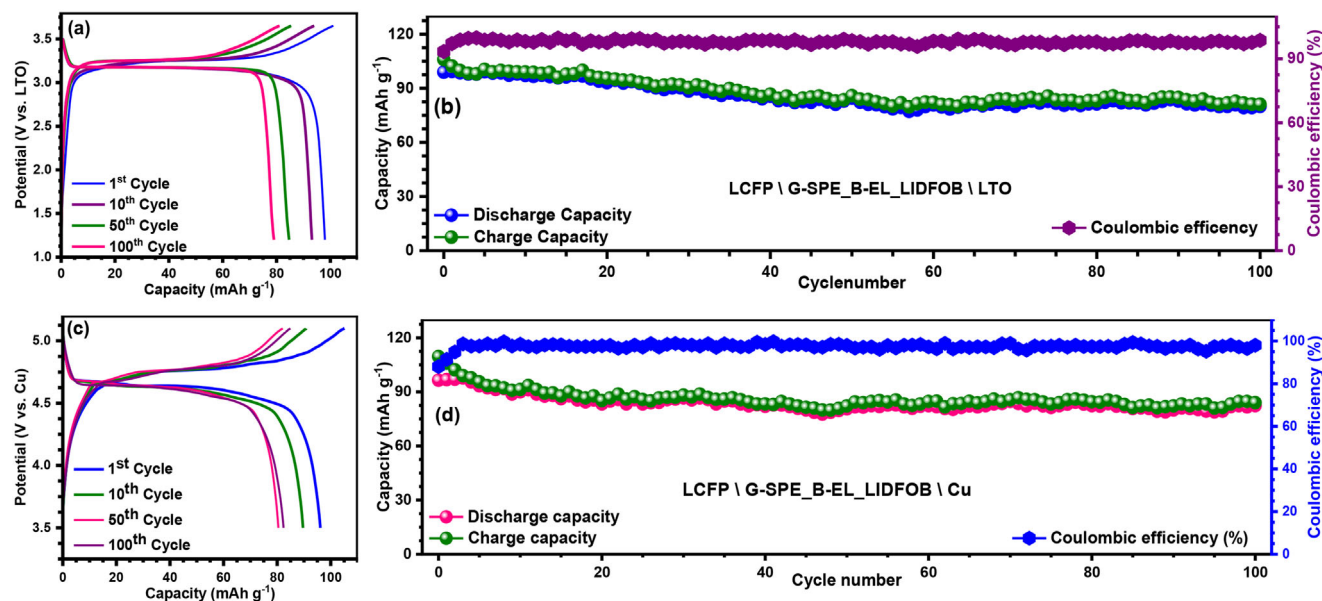


Figure 4. Charge–discharge plots and cycling profile data for a,b) LCFP\G-SPE_B-EL_LIDFOB\LTO, and c,d) LCFP\G-SPE_B-EL_LIDFOB\Cu.

by the F^- ions. Further, the optimized electrolyte combinations were further utilized for the full- and anode-less cell fabrication against LTO and Cu as counter electrodes.

4. Experimental Section

Synthesis of $LiCo_{0.9}Fe_{0.1}PO_4$: Carbon-coated $LiCo_{0.9}Fe_{0.1}PO_4$ was prepared by a solid-state synthesis method. In the initial step, stoichiometric amounts of the precursors such as Li_2CO_3 (Sigma-Aldrich), Co_3O_4 (Sigma-Aldrich), $(NH_4)_2HPO_4$ (Sigma-Aldrich), and Fe $(CH_3COO)_2 \cdot 2H_2O$ (Sigma-Aldrich) were mixed properly using a mortar and pestle. The precursor mixture was calcined in a box furnace to a temperature of 800 °C for a duration of 2 h to obtain the $LiCo_{0.9}Fe_{0.1}PO_4$. The as-obtained LCFP was then subjected to carbon coating. In the initial step of carbon coating, the $LiCo_{0.9}Fe_{0.1}PO_4$ was dispersed in deionized (DI) water containing glucose, where LCFP and glucose were mixed in a ratio of 2:1 (by weight). The solution was then subjected to slow heating to evaporate the water by keeping it at a temperature of 70 °C in a box furnace. The dried mixture was then recovered and calcined to a temperature of 800 °C for 2 h in a tube furnace in an Argon atmosphere. The $LiCo_{0.9}Fe_{0.1}PO_4@C$ was then subjected to high-energy ball-milling for a duration of 2 h to reduce the size and improve the Li-ion conduction. The as-prepared $LiCo_{0.9}Fe_{0.1}PO_4@C$ will be denoted as LCFP in the later sections. Here, a commercial sample of $LiNi_{0.5}Mn_{1.5}O_4$ (LNMO) was used for comparison.

Film Fabrication and Electrolyte Preparation: The SPE film was fabricated using a solution casting method. In the initial step, the polymer PVdF-HFP (Sigma Aldrich, $M_w \approx 4,00,000$) was dissolved in a binary mixture of acetone (Thermo Fisher) and tetrahydrofuran (volume ratio of 1:1). To the polymer solution, 1.5 wt.% of BN (Sigma-Aldrich, $\approx 1 \mu m$, 98%) was added as a filler and stirred properly for uniform dispersion. The solution was kept overnight for stirring, and the polymer mixture was coated onto a glass plate at a uniform thickness using a Doctor blade setup. The film was then peeled off from the glass plate and cut into circular pieces of uniform thickness. The SPE film was then kept overnight in a vacuum oven to remove any moisture content and soaked in a liquid electrolyte containing the initiator for free-radical polymerization for its percolation into the SPE film.^[31]

Different types of liquid electrolytes were prepared by dissolving $LiPF_6$ (Sigma-Aldrich,) in different solvents, such as ethylene carbonate (EC, Sigma-Aldrich, 98%), dimethyl carbonate (DMC, Sigma-Aldrich, $\geq 99.9\%$), ethyl methyl carbonate (EMC, Sigma-Aldrich, 99%), diethyl carbonate (DEC, Sigma-Aldrich, $\geq 99\%$), and additives such as lithium difluoro(oxalato)borate (LiDFOB, Sigma-Aldrich, $\geq 99.9\%$), fluoroethylene carbonate (FEC, Sigma-Aldrich, 99%). The prepared electrolyte combinations are- (a) 1M $LiPF_6$ dissolved in EC and DMC (1:1 by volume), G-SPE_B-EL, (b) 1M $LiPF_6$ dissolved in EC and DMC (1:1 by volume) with 5 wt.% of LiDFOB as an additive, G-SPE_LiDFOB, (c) 1M $LiPF_6$ dissolved in EC and DMC (1:1 by volume) with 5 wt.% of FEC as an additive, G-SPE_FEC, (d) 1M $LiPF_6$ dissolved in EC and EMC (1:1 by volume), G-SPE_EC-EMC, (e) 1M $LiPF_6$ dissolved in EC and DEC (1:1 by volume), G-SPE_EC-DEC. In all these electrolyte combinations, azobisisobutyronitrile (AIBN, Spectrochem) was added as a catalyst for radical initiation. All these solvents and salts are taken directly without any further purification.

Electrode Fabrication: The LCFP and LNMO electrodes were prepared by making a free-standing film. In this method, the active material, conductive carbon (Acetylene black, Alfa-aeser), and binder (TAB-2, teflonized acetylene black) were mixed in a ratio of 10:2:2 (in mg) using a mortar and pestle in ethanol medium. The mixing was continued until a free-standing film was obtained. The as-obtained film was then pressed on a stainless-steel mesh (14 mm, Goodfellow) using a hydraulic press (Specac, UK). The electrode was dried overnight in a vacuum oven at a temperature of 70 °C to remove the moisture content. The electrode was then inserted into a glovebox with O_2 and H_2O levels of <0.1 ppm, followed by cell fabrication in a CR2016 coin-cell setup using Li as a counter electrode. The fabricated coin cell was kept in a vacuum oven at a temperature of 70 °C to initiate liquid polymerization into a gel interface.

For the full-cell fabrication, $Li_4Ti_5O_{12}$ (LTO) was used as the anode. For the fabrication of the LTO electrode, a solution casting method was utilized. In this method, the LTO, conductive carbon (Acetylene black, Alfa-aeser), and PVdF (Alfa-aeser) were mixed in a ratio of 80:10:10 (by weight) in N-methyl pyrrolidone (NMP, Sigma-Aldrich) as solvent. The solvent was stirred overnight until it was mixed properly into a thick slurry. The electrode slurry was cast on an aluminum foil at a controlled thickness using a doctor blade setup. The foil was then kept in an oven for the solvent to evaporate, and the same was calendar-pressed and cut into microelectrodes of 14 mm diameter. The electrodes were then vacuum-dried overnight to remove any moisture content. The electrodes were then

inserted into a glovebox, followed by cell fabrication in a CR2016 coin-cell setup with LCFP as the cathode and LTO as an anode. Also, anode-less cell fabrication was carried out by fabricating LCFP against Cu as a counter electrode. The fabricated full- and anode-less cells were then kept in a vacuum oven for the radical polymerization to happen. The electrochemical studies of the full- and anode-less cells were performed at a potential window of 1.5–3.7 and 3.4–5.1 V vs. Li using a battery tester (Biologic, France).

Apart from the half-, full-, and anode-less cell fabrication, symmetric cells were fabricated to determine the transference number and analyze the stability of the electrolyte using the configuration Li\G-SPE\Li. Also, the symmetric cell of the configuration SS\G-SPE\SS (SS: spacer) was fabricated to determine the activation energy of the electrolytes. Further, asymmetric cells of the configuration Li\G-SPE\SS were fabricated to analyze the oxidation stability of the electrolyte using linear sweep voltammetry (LSV). All these studies were performed in the electrochemical workstation (Solartron) and battery tester (Biologic, France).

Material Characterizations: The X-ray diffraction analysis (XRD, Rigaku, Smart lab 9kW, monochromatic Cu K α radiation ($\lambda = 1.5406 \text{ \AA}$) has been carried out to analyze the phase and structure LCFP and G-SPE within a 2θ range of 10–90° at a scan rate of $0.1^\circ \text{ min}^{-1}$. The surface elemental composition of LCFP and the electrodes were analyzed using X-ray photoelectron spectroscopy (XPS) analysis. The surface area and pore size of the film were determined by BET (Quantachrome) analysis. Also, FE-SEM (ZEISS, Gemini 560) and TEM imaging were performed to analyze the morphology and size of the material.

Theoretical Studies: Density functional theory (DFT) calculations were performed to determine the electrochemical stability window of the electrolyte and additives using B3LYP functional and 6–31G basis set.

Supporting Information

Supporting Information is available from the Wiley Online Library or from the author.

Acknowledgements

S.S. acknowledges the Council of Scientific and Industrial Research (CSIR), Govt. of India for the fellowship. YSL acknowledges the financial support from the National Research Foundation of Korea (NRF) grant funded by the Korean government (Ministry of Science, ICT & Future Planning) (No. RS-2023-00208361). VA acknowledges financial support from the Anusandhan National Research Foundation (ANRF), Govt. of India, through Swarnajayanti Fellowship (SB/SJF/2020-21/12).

Conflict of Interest

The authors declare no conflict of interest.

Data Availability Statement

The data that support the findings of this study are available from the corresponding author upon reasonable request.

Keywords

anodeless, *ex situ*, high voltage, $\text{Li}_4\text{Ti}_5\text{O}_{12}$ anode, solid electrolytes

Received: March 17, 2025
Revised: May 20, 2025
Published online: June 24, 2025

- [1] A. Manthiram, *Nat. Commun.* **2020**, *11*, 1550.
- [2] A. Manthiram, *ACS Cent. Sci.* **2017**, *3*, 1063.
- [3] M. F. Sgroi, R. Lazzaroni, D. Beljonne, D. Pullini, *Batteries* **2017**, *3*, 11.
- [4] E. Markevich, R. Sharabi, O. Haik, V. Borgel, G. Salitra, D. Aurbach, G. Semrau, M. A. Schmidt, N. Schall, C. Stinner, *J. Power Sources* **2011**, *196*, 6433.
- [5] T.-F. Yi, J. Mei, Y.-R. Zhu, *J. Power Sources* **2016**, *316*, 85.
- [6] X.-Q. Zhang, X.-B. Cheng, X. Chen, C. Yan, Q. Zhang, *Adv. Funct. Mater.* **2017**, *27*, 1605989.
- [7] A. M. Haregewoin, A. S. Wotango, B. J. Hwang, *Energy Environ. Sci.* **2016**, *9*, 1955.
- [8] S. Sree Kumar, S. Natarajan, V. Aravindan, *Curr. Opin. Electrochem.* **2021**, *31*, 100868.
- [9] S. Sreedeeep, V. Aravindan, *Mater. Lett.* **2021**, *291*, 129609.
- [10] S. Sreedeeep, S. Natarajan, Y.-S. Lee, V. Aravindan, *Energy Technol.* **2023**, *11*, 2200988.
- [11] S. Sreedeeep, S. Natarajan, Y. S. Lee, V. Aravindan, *Electrochim. Acta* **2022**, *419*, 140367.
- [12] M. Zhang, N. Garcia-Araez, A. L. Hector, *J. Mater. Chem. A* **2018**, *6*, 14483.
- [13] G. Homann, L. Stolz, J. Nair, I. C. Laskovic, M. Winter, J. Kasnatscheew, *Sci. Rep.* **2020**, *10*, 4390.
- [14] V. van Laack, F. Langer, A. Hartwig, K. Koschek, *ACS Omega* **2023**, *8*, 9058.
- [15] P. Kodgire, B. Tripathi, P. Chandra, *J. Electron. Mater.* **2024**, *53*, 2203.
- [16] R. Ye, C. L. Tsai, M. Ihrig, S. Sevinc, M. Rosen, E. Dashjav, Y. J. Sohn, E. Figgemeier, M. Finsterbusch, *Green Chem.* **2020**, *22*, 4952.
- [17] C. Li, R. Li, K. Liu, R. Si, Z. Zhang, Y.-S. NaSICON Hu, *Interdiscip. Mater.* **2022**, *1*, 396.
- [18] A.-K. Hatz, R. Calaminus, J. Feijoo, F. Treber, J. Blahusch, T. Lenz, M. Reichel, K. Karaghiosoff, N. M. Vargas-Barbosa, B. V. Lotsch, *ACS Appl. Energy Mater.* **2021**, *4*, 9932.
- [19] Q. Wang, Y. Zhou, X. Wang, H. Guo, S. Gong, Z. Yao, F. Wu, J. Wang, S. Ganapathy, X. Bai, B. Li, C. Zhao, J. Janek, M. D. L. H. S. E. Wagemaker, *Nat. Commun.* **2024**, *15*, 1050.
- [20] K. H. Park, K. Kaup, A. Assoud, Q. Zhang, X. Wu, L. F. Nazar, *ACS Energy Lett.* **2020**, *5*, 533.
- [21] J. O. Dennis, M. F. Shukur, O. A. Aldaghri, K. H. Ibnaouf, A. A. Adam, F. Usman, Y. M. Hassan, A. Alsadig, W. L. Danbature, B. A. Abdulkadir, *Molecules* **2023**, *28*, 1781.
- [22] H. Bi, G. Sui, X. Yang, *J. Power Sources* **2014**, *267*, 309.
- [23] T. Wei, Z. Wang, Q. Zhang, Y. Zhou, C. Sun, M. Wang, Y. Liu, S. Wang, Z. Yu, X. Qiu, S. Xu, S. Qin, *CrystEngComm* **2022**, *24*, 5014.
- [24] S. Sreedeeep, Y. Lee, V. Aravindan, *J. Mater. Chem. A* **2025**, *13*, 13262.
- [25] Q. Hao, X. Ma, Y. Gao, F. Chen, X. Chen, Y. Qi, N. Li, *Energy Storage Mater.* **2024**, *70*, 103509.
- [26] J. Wu, X. Wang, Q. Liu, S. Wang, D. Zhou, F. Kang, D. Shanmukaraj, M. Armand, T. Rojo, B. Li, G. Wang, *Nat. Commun.* **2021**, *12*, 5746.
- [27] H. Wang, Y. Yang, C. Gao, T. Chen, J. Song, Y. Zuo, Q. Fang, T. Yang, W. Xiao, K. Zhang, X. Wang, D. Xia, *Nat. Commun.* **2024**, *15*, 2500.
- [28] F. Yu, L. Zhao, H. Zhang, Z. Sun, Y. Li, Q. Hu, Y. Chen, *RSC Adv.* **2021**, *11*, 3854.
- [29] T. Chen, C. Zhao, T. Lai, J. Zhao, *Polym. Chem.* **2025**, *16*, 903.
- [30] T. Zhang, Q. Yang, Z. Wu, T. Chen, F. Wan, L. Qiu, B. Zhong, Y. Chen, X. Guo, *Chem. Eng. J.* **2025**, *509*, 160818.
- [31] S. Sreedeeep, Y.-S. Lee, V. Aravindan, *Small* **2025**, <https://doi.org/10.1002/sml.202503594>.
- [32] S. Sreedeeep, S. Praneetha, Y.-S. Lee, V. Aravindan, *ChemElectroChem* **2022**, *9*, 202200815.
- [33] S. Sreedeeep, Y.-S. Lee, V. Aravindan, *Adv. Sustainable. Syst.* **2023**, *7*, 2300267.
- [34] S. Sree Kumar, S. Natarajan, Y.-S. Lee, V. Aravindan, *Energy Technol.* **2022**, *11*, 2200988.

- [35] S. Sreedeeep, Y.-S. Lee, V. Aravindan, *Compos. Part B Eng.* **2024**, 277, 111365.
- [36] J. Cha, J. G. Han, J. Hwang, J. Cho, N. S. Choi, *J. Power Sources.* **2017**, 357, 97.
- [37] P. Karayaylali, Y. Zhang, L. Giordano, Y. Katayama, R. Tatara, Y. Yu, F. Maglia, R. Jung, Y. Shao-Horn, *J. Electrochem. Soc.* **2020**, 167, 040522.
- [38] M. Nie, J. Demeaux, B. T. Young, D. R. Heskett, Y. Chen, A. Bose, J. C. Woicik, B. L. Lucht, *J. Electrochem. Soc.* **2015**, 162, A7008.